6

Principles and Applications of the qPlus Sensor

Franz J. Giessibl

> Man sollte die Dinge so einfach wie möglich machen, aber nicht einfacher.
>
> *(Things should be made as simple as possible, but not one bit simpler.)*
>
> Albert Einstein (1879–1955)

Abstract. The concept of the atomic force microscope (AFM) is a very simple one: map the surface of a sample by a sharp probe that scans over the surface similar to the finger of a blind person that reads Braille characters. In AFM, the role of that finger is taken by the probe tip that senses the presence of the sample surface by detecting the force between the tip of the probe and a sample. The qPlus sensor is a self sensing cantilever based on a quartz tuning fork that supplements the traditional microfabricated cantilevers made of silicon. Quartz tuning forks are used in the watch industry in quantities of billions annually, with the positive effects on quality and perfection. Three properties of these quartz-based sensors simplify the AFM significantly: (1) the piezoelectricity of quartz allows simple self sensing, (2) the mechanical properties of quartz show very small variations with temperature, and (3) the given stiffness of many quartz tuning forks is close to the ideal stiffness of cantilevers. The key properties of the qPlus sensor are a large stiffness that allows small amplitude operation, the large size that allows to mount single-crystal probe tips, and the self-sensing piezoelectric detection mechanism.

6.1 Motivation: qPlus Versus Si Cantilever

The first atomic force microscope utilized a cantilever that was built by hand in the laboratory from gold foil and a small piece of diamond acting as a tip [1]. Soon after, MEMS (micro electronic and mechanical systems) capabilities offered by the semiconductor industry were utilized to mass-fabricate cantilevers from silicon.

S. Morita et al. (eds.), *Noncontact Atomic Force Microscopy*,
NanoScience and Technology,
DOI: 10.1007/978-3-642-01495-6_6,

Initially, Si-based cantilevers were built from SiO_2 and Si_3N_4 [2]. Later, cantilevers with integrated tips were machined from silicon-on-insulator wafers [3]. The most common cantilevers in use today are built from all-silicon with integrated tips pointing in a [001] crystal direction and go back to Wolter et al. [4], followed by a number of companies that offer Si cantilevers with integrated sharp tips on wafers, including a few hundred cantilevers each.

The qPlus sensor still requires manual assembly and it is fair to ask why two decades after the introduction of AFM, manual assembly of its key component is still practiced. Manual assembly was even practiced in manufacturing transistors years after its invention [5] – the reason why manual production of cantilevers is still warranted is outlined in this chapter.

6.1.1 Specifications of an Atomic Force Probe

Imagine the ideal properties of that tiny finger that should probe a surface without destructing it. One first obvious quality of that probe is to be very sharp that ideally a single atom sits at its end. Second, the probe needs to be sensitive enough to be able to feel the tiny forces that act between single atoms. The first AFMs were mostly operated in "contact" mode, and for this mode the stiffness of the cantilever should be significantly smaller than the interatomic spring constants of atoms in a solid [6], which amounts to $k \leq 10\,\mathrm{N\,m^{-1}}$. For nondestructive imaging, the forces between tip and sample should be small compared to the maximal forces that can be sustained by single bonds. Also, it is desired to keep artifacts due to elastic deformations of tip and sample small [7]. It has to be kept in mind, though, that elastic effects will occur in imaging. There is a tradeoff between maximizing the signal-to-noise level by imaging at very close distances and by minimizing tip and sample distortion by imaging at large distances where forces are small. This tradeoff can be somehow relaxed by reducing the noise level in the force measurements – a pursuit that pervades all progress in AFM.

Figure 6.1 shows a schematic view of a probe tip close to a sample. The bonds within the sample (and similar the bonds within the probe tip) have a stiffness k_{ss}, which amounts to roughly $170\,\mathrm{N\,m^{-1}}$ in the case of silicon. The bond between the front atom of the tip and the sample atom next to it is depicted by k_{ts}, which strongly depends on the distance between tip and sample.

For an illustration of the magnitude of typical tip sample bonds, we use the Stillinger–Weber potential [8] that has been devised to describe the bonding in silicon. The Stillinger–Weber potential not only depends on the distance between two silicon atoms, but also on the mutual alignment of next nearest neighbor atom. In the case of perfect tetragonal bonding symmetry, the bonding energy $V_{\mathrm{Si-Si}}$, the force $F = -\partial V_{\mathrm{Si-Si}}/\partial z$ and stiffness $k_{\mathrm{Si-Si}} = \partial^2 V/\partial z^2$ is only a function of the interatomic distance z. These functions are shown in Fig. 6.2. The Stillinger–Weber potential is often used as a model for describing covalent bonds, but it has some constraints. A very serious constraint

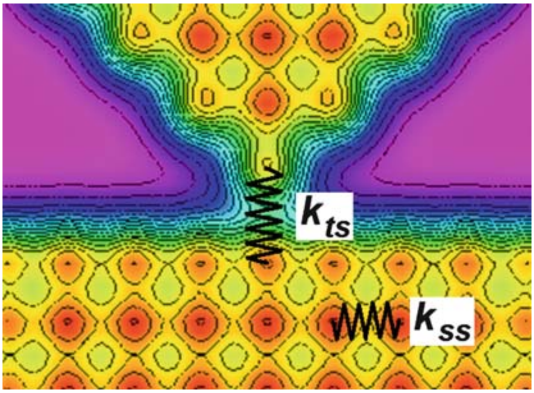

Fig. 6.1. A sharp tip close to a sample. The bonds of the atoms in tip and sample are characterized by a stiffness k_{ss}. For silicon, $k_{\mathrm{ss}} \approx 170\,\mathrm{N\,m^{-1}}$. The stiffness of the "bond" between the front atom of the tip and the sample atom next to it is given by k_{ts}, which strongly depends on the tip sample distance

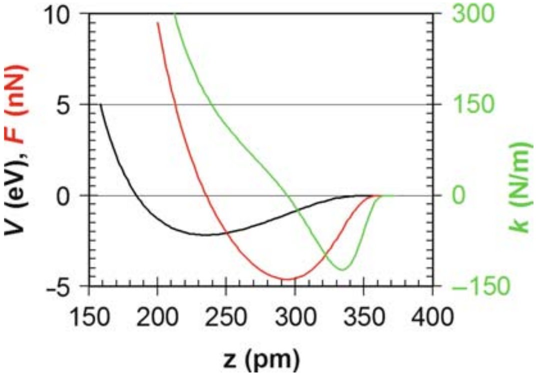

Fig. 6.2. Potential energy V, force F, and stiffness k for a single Si–Si bond after the Stillinger–Weber potential. The potential reaches its minimum of $-2.17\,\mathrm{eV}$ for an equilibrium distance of $z_{\mathrm{eq}} = 235\,\mathrm{pm}$. The maximum attractive force reaches $-4.6\,\mathrm{nN}$ at a distance of 296 pm and the stiffness at z_{eq} is $k_{\mathrm{eq}} = 170\,\mathrm{N\,m^{-1}}$. For distances $z > 296\,\mathrm{pm}$, the stiffness k_{ss} is negative, reaching a minimal value of $-120\,\mathrm{N\,m^{-1}}$

is the artificial limitation of the bonding length to 376 pm – the potential is assumed to be zero for greater distances. The key reason for that is that the nearest neighbors in Si are 384 pm apart, and the calculation of lattice energies becomes simpler if only the nearest neighbors have to be taken into account. This artificial limitation causes the rather strong maximal attractive force of more than $-4\,\mathrm{nN}$ and the rather large force gradient of $-120\,\mathrm{N\,m^{-1}}$. Nevertheless, the Stillinger–Weber potential describes the experimental phonon spectrum of Si very well and even though the actual Si bonds may be somewhat weaker (see, e.g., total energy pseudopotential calculations by Perez et al. [9]) it has to be anticipated that single atomic bonds in semiconductors have a stiffness on the order of $\pm 100\,\mathrm{N\,m^{-1}}$. The stiffness of bonds in solids can be estimated from the frequencies of optical phonons [10]. Silicon has an optical phonon at a wavenumber of $520\,\mathrm{cm^{-1}}$ (at the Gamma point where $\boldsymbol{k} = 0$), every Si atom in the bulk is embedded in bonds with an effective spring constant of $447\,\mathrm{N\,m^{-1}}$. Diamond, in contrast, has an optical phonon at a wavenumber of $1{,}200\,\mathrm{cm^{-1}}$ and every C atom in diamond is embedded in bonds with an effective spring constant of $1{,}020\,\mathrm{N\,m^{-1}}$. This value is very high compared to the stiffness of the mainly used commercial silicon cantilevers.

6.1.2 Cantilevers in Dynamic Force Microscopy

In dynamic force microscopy, the cantilever is oscillating and amplitude changes [11] or frequency shifts [12] are utilized to probe the forces acting between tip and sample. Atomic resolution on reactive surfaces was first obtained in frequency modulation AFM with very large cantilever oscillation amplitudes of 34 nm [19]. Initially, it was not clear why these huge amplitudes were required, but the simple picture shown in Fig. 6.3 explains that situation.

The eigenfrequency f_0 of the cantilever is given by

$$f_0 = \frac{1}{2\pi}\sqrt{\frac{k}{m}}, \tag{6.1}$$

and when the stiffness of the tip sample bond k_{ts} is taken into account, the new frequency is

$$f = \frac{1}{2\pi}\sqrt{\frac{k + k_{\mathrm{ts}}}{m}}. \tag{6.2}$$

Equation (6.2) is correct only if k_{ts} is constant during the oscillation cycle. For large amplitudes, this is certainly not the case.

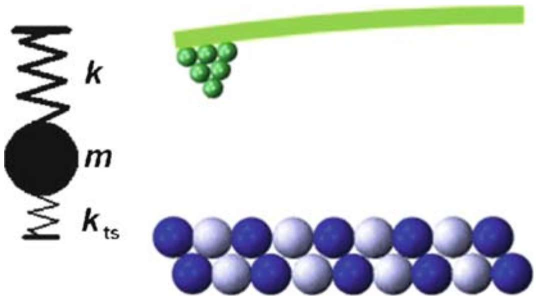

Fig. 6.3. Mass and spring model (*left*) as a mechanical analog of an oscillating cantilever next to a surface (*right*)

When the oscillation amplitude A is large, we have to generalize (6.2) by

$$f = \frac{1}{2\pi}\sqrt{\frac{k + \langle k_{\mathrm{ts}}\rangle}{m}}. \tag{6.3}$$

When $\langle k_{\mathrm{ts}}\rangle$ is small compared to k, we can express the frequency shift $\Delta f = f - f_0$ as

$$\Delta f(z) = f_0 \frac{\langle k_{\mathrm{ts}}(z)\rangle}{2k}, \tag{6.4}$$

with

$$\langle k_{\mathrm{ts}}(z, A)\rangle = \frac{2}{\pi}\int_{-1}^{1} k_{\mathrm{ts}}(z - Au)\sqrt{1-u^2}\,\mathrm{d}u. \tag{6.5}$$

Also, we note that for small tip sample distances, k_{ts} can become quite large (see Fig. 6.2). In this case, the stiffness of the cantilever k would need to be significantly larger than $100\,\mathrm{N\,m^{-1}}$; otherwise, stable oscillation would become impossible [14]. In frequency modulation AFM, the cantilever is part of an oscillator that has to oscillate at a precisely determined amplitude A, as any amplitude fluctuations show up as noise in the AFM data. The creation of a stable oscillator is difficult enough (for a block diagram of the oscillator circuit of an FM-AFM, see, e.g., [15]) and stability is easier to obtain if the oscillation frequency does not vary too much around f_0, in other words, we demand that $\mid \Delta f \mid \ll f_0$ thus $\mid \langle k_{\mathrm{ts}}\rangle \mid \ll k$. For small amplitude operation, $\langle k_{\mathrm{ts}}\rangle \approx k_{\mathrm{ts}}$ and thus we demand that $k \gg \mid k_{\mathrm{ts}} \mid$.

6.1.3 Advantages of Small Amplitude Operation

In the scanning tunneling microscope (STM), the tunneling current is used to probe the presence of a sample surface. As the tunneling current increases by a factor of ten for every distance reduction of 100 pm, there is only one current path that mainly originates from the front atom of the tip. In AFM, forces of various origin are acting on the probe of the tip, but ideally only the short range contributions originating from the front atom would be measured. In frequency modulation AFM, there is a way to discriminate force contributions by their decay length. In large amplitude AFM, it has been shown that the frequency shift is dominated by long-range forces. The normalized frequency shift γ, which is defined by

$$\gamma := \frac{\Delta f}{f_0} k A^{3/2}, \tag{6.6}$$

can be expressed as

$$\gamma \approx 0.4 \times \sum_{i=1}^{N} F_{\mathrm{ts}}^{i}\sqrt{\lambda_i}, \tag{6.7}$$

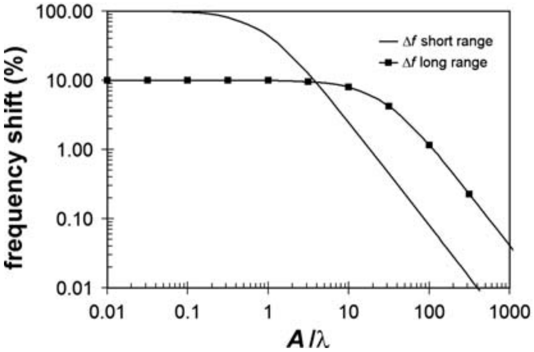

Fig. 6.4. Frequency shift contributions of short- and long-range force components as a function of amplitude

where i is an index denoting the force channel. For example, let us assume the interaction consists of a short range force with a magnitude of 1 nN and a range of 100 pm and a long range force with a magnitude of 3 nN and a range of 3 nm. The long-range forces are mainly caused by van der Waals interactions that can be reduced by using sharp tips [16–18]. In this case, the contribution of the long-range force to the frequency shift is $3 \times \sqrt{30} \approx 16$ times as large as the short range contribution.

For oscillation amplitudes that are small compared to the range of the short-range interaction λ, the frequency shift is proportional to the force gradient (see (6.4)) and the long-range contribution is only 10% of the short-range contribution. The crossover from small- to large amplitude operation is shown in Fig. 6.4. This figure shows how the frequency shift becomes smaller as the amplitude is increased. It is important to note that the minimum distance (lower turnaround point of the cantilever) is held constant when the amplitude is varied. When the amplitude reaches the range of the short-range interaction λ, the frequency shift component originating from the short range force starts to decrease while the long-range component still remains constant. For $A \approx 3 \times \lambda$, the contributions of long- and short-range force match, while for $A > 3 \times \lambda$, the long-range contributions dominate Δf. In summary, large amplitude FM-AFM requires the use of very sharp tips, while small amplitude AFM can cope with blunt tips as well.

The cost of using small amplitudes is an increase in frequency noise. Albrecht et al. [12] have calculated the thermal noise of a cantilever and found

$$\frac{\delta f_{\text{thermal}}}{f_0} = \sqrt{\frac{k_B T B}{\pi f_0 k A_{\text{rms}}^2 Q}}, \tag{6.8}$$

that is, the thermal noise ratio is roughly given by the square root of the ratio between the thermal energy $k_B T$ and the mechanical energy stored in the cantilever $kA^2/2$ divided by the quality factor Q and multiplied by the ratio between bandwidth and frequency ($A^2 = 2A_{\text{rms}}^2$).

Often times, the thermal noise is smaller than the detector noise. Detector noise is described by the precision at which we can measure the cantilever deflection. Good interferometers as well as electrical detection of the qPlus deflection reach deflection noise densities of $n_{q'} = 100\,\mathrm{fm}/\sqrt{\mathrm{Hz}}$. A deflection noise density of $n_{q'} = 100\,\mathrm{fm}/\sqrt{\mathrm{Hz}}$ means that the position of the cantilever can be determined with a precision of 100 fm in a 1 Hz bandwidth and with a 1 pm deflection noise for a bandwidth of 100 Hz.

The corresponding frequency noise is [19, 20]

$$\frac{\delta f_{\mathrm{detector}}}{f_0} = \frac{n_{q'}}{\pi A f_0} B_{\mathrm{FM}}^{3/2}, \tag{6.9}$$

where B_{FM} is the bandwidth of the frequency detector. Because the two noise sources are statistically independent, we find

$$\delta f = \sqrt{\delta f_{\mathrm{thermal}}^2 + \delta f_{\mathrm{detector}}^2}. \tag{6.10}$$

Here it is important that detector noise increases dramatically with B_{FM}; therefore, slow scanning reduces noise sharply. Both thermal and detector frequency noise vary inversely with amplitude. The signal-to-noise ratio is thus given by dividing the signal level shown in Fig. 6.4 by the $1/A$ dependence of the frequency noise. The result is displayed in Fig. 6.5. The signal-to-noise ratio is optimal when the amplitude is tuned to the interaction that is to be used for imaging. In the first application of FM-AFM [12], magnetic dipole forces on recording media have been probed and the use of large amplitudes was helping to obtain good quality images. However, the analysis above shows that for probing atomic interactions with force ranges in atomic dimensions, amplitudes in the 100 pm range are preferred.

The use of small amplitude suppresses long-range contributions to the frequency shift and optimizes the signal-to-noise ratio.

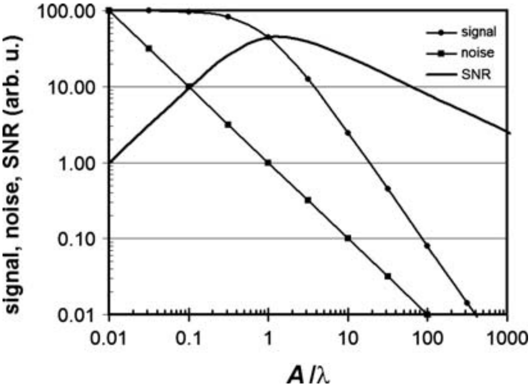

Fig. 6.5. Signal-to-noise ratio (SNR) in FM-AFM as a function of amplitude

6.1.4 Ideal Physical Properties of Cantilevers

Three physical properties of cantilevers are relevant in force microscopy:

1. Stiffness k
2. Eigenfrequency f_0
3. Quality factor Q

Because of the considerations outlined in Sect. 6.1.2, we want the stiffness k to be on the order of $1\,\mathrm{kN\,m^{-1}}$ to allow stable small amplitude operation.

The eigenfrequency f_0 should be as high as possible to minimize frequency noise (see (6.9) and (6.8)). However, there is a tradeoff that depends on the specific implementation of the deflection sensor. Usually, the deflection noise $n_{q'}$ increases with frequency for a given detector and so the optimal value depends on the detection method.

The quality factor Q should be as high as possible, according to (6.8). However, there is a practical consideration. One way to express the quality factor is to compare the energy loss per cycle $\Delta E_{\mathrm{cycle}}$ in a damped oscillator to the energy stored in the cantilever $E = kA^2/2$:

$$Q = \frac{2\pi E}{\Delta E_{\mathrm{cycle}}}. \tag{6.11}$$

If Q is extremely large, amplitude control can become very difficult because the interaction of the probe tip with a sample is in general dissipative and the relative change of the energy loss per cycle is inversely proportional to Q.

In practice, it is also important how these parameters depend on the medium (liquid, gaseous, vacuum) and temperature. One of the main reasons why frequency standards are often built from quartz tuning forks is their superiority to silicon with respect to frequency stability vs. temperature [21]. Also, for practical considerations, it is very important to consider the type of probe tips that can be used with a given cantilever.

6.2 Theory of qPlus Versus Tuning Fork Sensors

Quartz tuning forks are wonderful inventions. They allow to produce watches at very low cost that keep time much more precise than mechanical watches that are prized orders of magnitude higher [22]. Here, we explain the principle of quartz tuning forks and explain how they can be rebuilt to act as powerful force sensors.

6.2.1 Quartz Tuning Forks

Quartz tuning forks are etched from single crystal quartz that is oriented in a $X + 5^\circ$ orientation [23]. This orientation ensures that the frequency variation

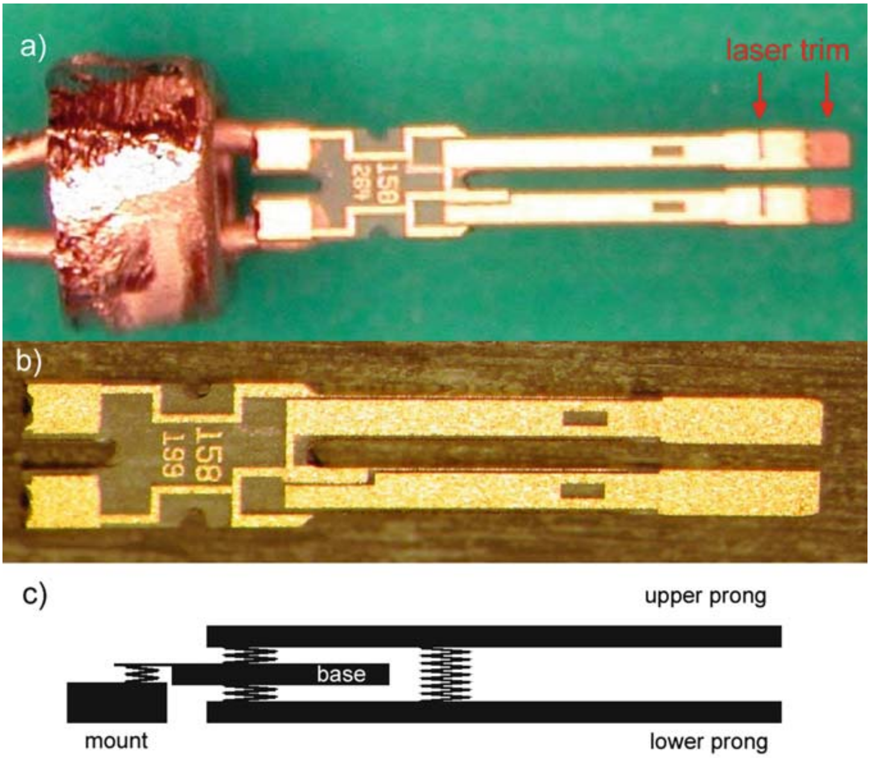

Fig. 6.6. Quartz tuning forks. (**a**) A tuning fork as used in watches with an opened metal case. The arrows point to an area where the gold plating has been partially removed to trim the mass of the prongs such that an eigenfrequency of exactly 32,768 Hz arises. (**b**) Untrimmed tuning fork as taken out of a wafer. The trimming procedure has not been done on this fork as can be seen by the undamaged gold plating at the end of the fork. (**c**) Mechanical analog of the tuning fork: in principle, the fork is a quite complex mechanical system with many oscillation modes and eigenfrequencies. When both prongs are symmetric, the antiparallel mode where one prong oscillates opposite to the other one has a very high Q value

with temperature is almost zero at 28° C – the typical temperature of a watch mounted on a wrist. The piezoelectricity of quartz allows for a simple transformation of the mechanical oscillation of the quartz fork to an electrical signal. Incidentally, the piezoelectric effect and its inversion that are instrumental for the whole field of scanning probe microscopy have been first observed in quartz by the Curie brothers (see the instructive report in Chen's introduction to STM [76]). Quartz tuning forks have surprisingly large Q-values – on the order of 10^5. Therefore, frequency stability is excellent and power consumption is very low – ideal for watch applications. Figure 6.6a shows a quartz tuning fork as used in Swatch watches. The metal case of the device has been opened

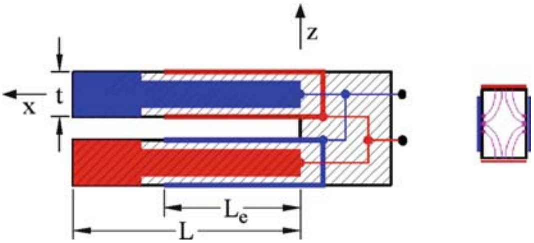

Fig. 6.7. Electrode configuration of the quartz tuning forks shown in Fig. 6.6

and one can see the transparent quartz fork as well as the gold electrodes. The gold electrodes have been removed partially at the ends of the prongs to adjust the eigenfrequency to exactly 2^{15} Hz (32.768 kHz). Figure 6.6b shows a similar tuning fork that has not yet been trimmed. The prongs are rectangular and are surrounded by gold electrodes – two vertical and two horizontal layers of gold (see Fig. 6.7). Figure 6.6c is a mechanical analog to the tuning fork. When both prongs have exactly the same mass and stiffness, an oscillation mode where both prongs oscillate opposite to each other evolves that has extremely little losses and thus with (6.11) a very high Q value.

Because of their useful properties, quartz tuning forks have been applied in scanning probe microsocopy quite early. Guethner et al. [25] has used a quartz tuning fork for scanning near field acoustic microscopy, and Karrai et al. [26] used tuning forks to sense the distance of near field optical microscopes. Rychen has used tuning forks to probe forces in low temperatures and high magnetic fields [27–29]. However, the high symmetry of tuning forks has to be given up when a probe is attached to one of the prongs as required for using the fork as a sensor. Dransfeld et al. [30] have proposed to attach a counterweight to the prong that does not carry a tip, and Rychen et al. use extremely lightweight tips [29]. The influence of adding mass to one of the prongs on the Q value has been analyzed in Rychen's Ph.D. thesis [31] and it is found that the Q-value drops considerably when the added mass reaches about 1% of the mass of one prong. The piezoelectric effect results in the generation of surface charges upon mechanical stress. To convert the mechanical stress within the prongs of the tuning forks into surface charges that are collected by metal electrodes on the quartz material, two designs are in use: thick prongs where the width w (y-coordinate in Fig. 6.7) and the thickness t (z-coordinate in Fig. 6.7) of the cross-section of one prong are on the same order of magnitude and thin prongs where the thickness is much greater than the width [23]. For thick prongs such as the ones shown in Fig. 6.6, the electrode configuration is usually as shown in Fig. 6.7. The cross section in the right side of Fig. 6.7 shows the electrodes and the electric field lines within the quartz material. When one beam of the fork is deflected by an amount z, the charge q that is collected on the electrode is given by

$$q = z d_{21} k L_\mathrm{e}(L_\mathrm{e}/2 - L)/t^2, \tag{6.12}$$

where d_{21} is the piezoelectric coupling constant ($d_{21} = 2.31\,\mathrm{pC\,N^{-1}}$ for quartz), k is the spring constant, L_e is the length of the electrodes (see Fig. 6.7), L is the length of the prongs, and t is the thickness of the prongs [32]. The sensitivity of the E158 fork shown here is $q/z = 2.8\,\mathrm{\mu C\,m^{-1}}$.

Two observations deserve to be mentioned: (a) the sensitivity is proportional to the spring constant and (b) the electrodes do not need to reach until the very end of the fork to get good sensitivity – for $L_\mathrm{e} = 0.8L$ we still get 96% of the maximum sensitivity at $L_\mathrm{e} = L$. Thus we can afford to leave the end of the prongs free of electrodes for contacting a tip.

For the type of forks used here, the dimensions are given by $L = 2.4\,\mathrm{mm}$, thickness $t = 214\,\mathrm{\mu m}$, and width $w = 130\,\mathrm{\mu m}$. The theoretical stiffness of one beam is given by

$$k = \frac{1}{4} E w \frac{t^3}{L^3}, \tag{6.13}$$

where E is the elastic modulus ($E = 78.7\,\mathrm{GPa}$ for quartz) and w is the width of the prongs. The formula is derived for a beam that is fixed to massive material. In the tuning fork configuration, a slightly smaller spring constant is expected. Heyde et al. [33] have performed finite element analysis to calculate the expected spring constant. Here, we follow a different approach: the quantities that can be measured with great precision are w and L. In contrast, it is harder to measure t. The frequency f_0 can be measured with great precision. For a clamped beam, f_0 is given by [76]

$$f_0 = 0.161 \sqrt{\frac{E}{\rho}} \frac{t}{L^2}, \tag{6.14}$$

where ρ is the mass density ($\rho = 2{,}650\,\mathrm{kg\,m^{-3}}$ for quartz). Thus, we can use (6.14) to measure the effective thickness t and get a more precise value for k. For the forks we use here the theoretical spring constant is $k = 1{,}800\,\mathrm{N\,m^{-1}}$.

6.2.2 qPlus Sensor

Even when the mass of a tip attached to one of the prongs is compensated by attaching a similar mass to the other prong, the asymmetry that affects the prong that interacts with a surface cannot be lifted easily. Therefore, we attach one prong to a heavy substrate such that we end up with a quartz cantilever instead of a quartz tuning fork. Even the use of heavy tips or a strong interaction with a surface bond will not cause a collapse of the Q factor. Therefore, we call this arrangement the qPlus sensor configuration as opposed to a tuning fork configuration [34, 35]. Essentially, the qPlus sensor is a cantilever made of quartz with various favorable properties

1. A stiffness close to the optimal value as found in Sect. 6.1
2. A high Q value
3. Self sensing

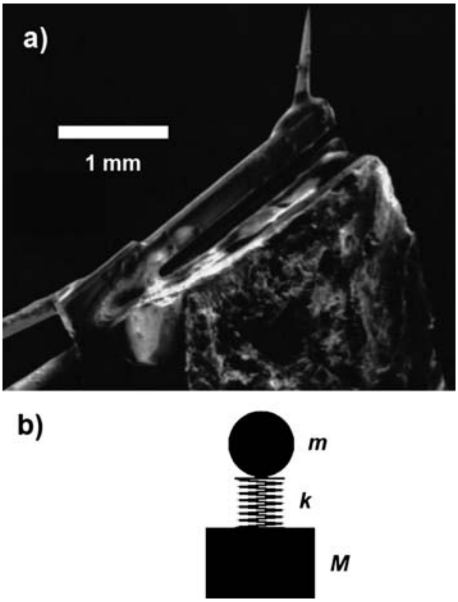

Fig. 6.8. A quartz tuning fork is glued onto a heavy substrate, turning the tuning fork into a qPlus sensor. In this first prototype of a qPlus sensor shown in (**a**), the free prong of the tuning fork is glued to a piece of Pyrex glass. The tip is an etched tungsten wire with a wire diameter of approx. 200 µm. The mechanical analog to the qPlus sensor is shown in (**b**). It is much simpler than in the case of the tuning fork, because only the free prong is allowed to oscillate. The mass of the mount M should be large compared to the effective mass of the fork, where $M > 1{,}000\,m$ is a reasonable value

The sensor shown in Fig. 6.8 has been used for high speed imaging in ambient conditions [36]. The electrical connections of the fork were connected to an instrumentation amplifier with a high gain. The charges that are collected on the electrodes when the sensor is deflected cause a voltage change in the input of an instrumentation amplifier. The charges q that collect on the electrodes change the potential difference at the input terminal.

6.2.3 Manufacturing High Quality qPlus Sensors

After the proof of principle was reached, the resolution limits that could be probed with the new sensor were investigated. First, the manufacture of the sensor needed to be simplified. On that behalf, a ceramic substrate that simplifies the building of the sensor was designed. The substrate is made of alumina with vias and conductive leads as well as mounting holes. Substrates of this kind are used in hybrid electronics design and can be ordered as custom designs [37].

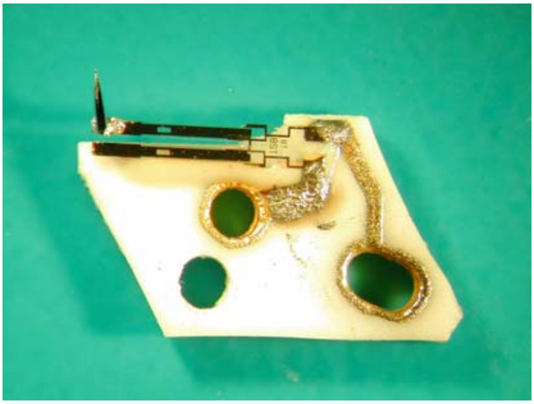

Fig. 6.9. Second generation qPlus sensor. The sensor consists of three parts: the tuning fork, a ceramic substrate, and the tip. Electrical connections are made using conductive epoxy [38]

Fig. 6.10. Third generation qPlus sensor. A different ceramic substrate is used that allows to isolate the tip potential from the electrodes of the sensor. The tip is contacted with a squeezed gold wire (diameter 10 µm). The Q-value still remains on the order of a few thousand. The two electrodes of the tuning fork are fed into a single amplifier, see Sect. 6.2.4

To obtain a sensor with a high Q-value, it is important to create a very stiff bond between the fork and the substrate. This can be achieved by using a very thin layer of glue and by taking care that the area where the free prong meets the base part of the fork remains free of glue (see Fig. 6.9). This sensor design can also be used to build a lateral force sensor by rotating the tip by 90° and oscillating the tip parallel to the surface [39]. The third generation of qPlus sensors is shown in Fig. 6.10. Here, the tip is connected via a dedicated terminal. This allows to apply high voltages for tip annealing or field emission without affecting the deflection sensors amplifiers. Both electrodes of the fork

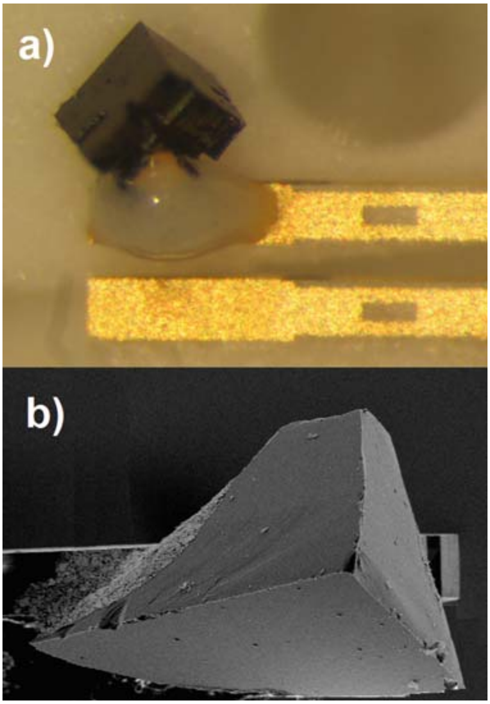

Fig. 6.11. Single-crystal tips for the qPlus sensor. (**a**) NiO single crystal tips for in situ cleavage. The cuts in the crystal are designed to facilitate cleaving such that a tip with three freshly cleaved NiO {001} surfaces arises [41]. (**b**) Si single crystal tips for ex situ cleavage. An Si tip terminated by three {111} faces emerges [42, 43]

are fed into a current-to-voltage amplifier and the difference between the two signals has much less interference noise than a single deflection electrode. [40]

The tip of the force sensor is a crucial part. Ideally, we want a single atom at the front with a well defined atomic neighborhood. A single crystal tip appears to be ideal. Tips from silicon have been cleaved ex situ, exposing three {111} faces [42,43]. NiO tips that are bound by {001} cleaved ex situ [44] and in situ [41] have been created as well.

6.2.4 Preamplifiers for qPlus Sensors

The qPlus sensor needs only one more component to produce an electrical deflection signal: a current-to-voltage converter that converts the flowing charges generated at the oscillating prongs into a voltage. Because cable capacity has an adverse effect on the noise performance of the deflection measurement, the amplifier should be located as close as possible to the sensor. For vacuum and low-temperature applications, it is challenging to design an amplifier that is compatible with these demanding environments.

Figure 6.12 shows the evolution of amplifiers we went through. The first type shown in Fig. 6.12a is an instrumentation amplifier. This type was used in the first qPlus experiments in ambient environments. The principle of operation is the following: when the qPlus sensor is deflected, charges accumulate on the electrodes as given in (6.12). These charges cause a voltage increase in the capacitor (qPlus electrodes plus cable capacity) and the voltage differential is measured with the instrumentation amplifier. To define the input potentials of the instrumentation amplifier and to avoid long-term charging effects, the inputs need to be connected to ground with a very large resistivity (at least 100 MΩ).

The second type shown in Fig. 6.12b) is a traditional transimpedance amplifier as used in current amplifiers of STMs. To obtain a high bandwidth, it is important to use a resistor that has little stray capacitance. Surface-mount-device (SMD) resistors work well here. The case of the amplifier should be vacuum compatible, for example, the amplifier should be available in a metallic or ceramic case, although we have used plastic cases in UHV without

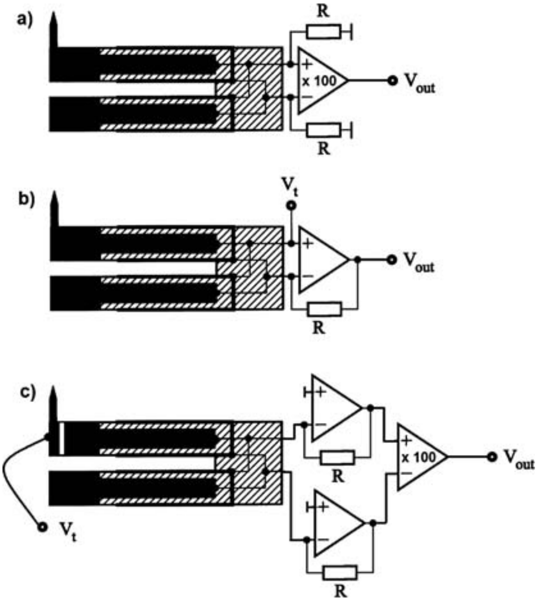

Fig. 6.12. Three types of preamplifiers for qPlus sensor. (**a**) First generation, an instrumentation amplifier (AD 624 [45]) with two resistors. (**b**) Second generation, a current-to-voltage converter or transimpedance amplifier, similar to the ones used in STM current amplification. Operational amplifiers that work well here are the AD711, AD744, and AD823 [45]. (**c**) Third generation, a dual current-to-voltage converter with an instrumentation amplifier (e.g., AD823 for the I/V converter and AD624 as an instrumentation amplifier). The resistor values are all on the order of 100 MΩ, with a small and low capacity SMD design

apparent additional outgassing and adverse effects on vacuum pressure. In STM, a bandwidth B_{IVC} of 1 kHz is usually sufficient, but here we need at least 10 kHz. Assuming an ideal operational amplifier, the gain of the amplifier is given by

$$V_{\mathrm{out}} = \frac{I_{\mathrm{in}}R}{1 + \mathrm{i}2\pi fRC}, \qquad (6.15)$$

where R is the feedback resistor and C is its stray capacitance.

Proper heat sinking is important if the amplifier operates in vacuum, especially if small cases are used, because the cooling effect of air is of course missing in vacuum. Generally, it is a good idea to operate the amplifiers close to the lower threshold of the operating voltage to minimize heat introduction caused by the electric power that is consumed in the amplifier. To avoid uncontrolled oscillations ("motor boating" [46]), it is advisable to put buffer capacitors close to the power terminals of the operational amplifier [47].

The third type of preamplifier shown in Fig. 6.12c uses two channels for the deflection measurement. The advantage of this approach is that the signal becomes twice as large, and uncorrelated noise is only a factor of $\sqrt{2}$ larger and so an increase in signal-to-noise ratio of $\sqrt{2}$ is expected. Correlated noise, such as interference noise, even cancels completely because of the differential stage at the output of the two current amplifier channels. Also, the tip bias is completely free, allowing high-voltage tip treatment or field emission while the sensor is attached to the microscope [40].

Figure 6.13 shows an amplifier in the most demanding environments: vacuum and low temperatures. The operational amplifier in use is of type AD823 [45]. This device can be reliably operated with a very low voltage of ±1.5 V at a quiescent current of typically 5 mA. At low temperatures and 3 V operating voltage, the current is only about 2 mA, thus the heat production is

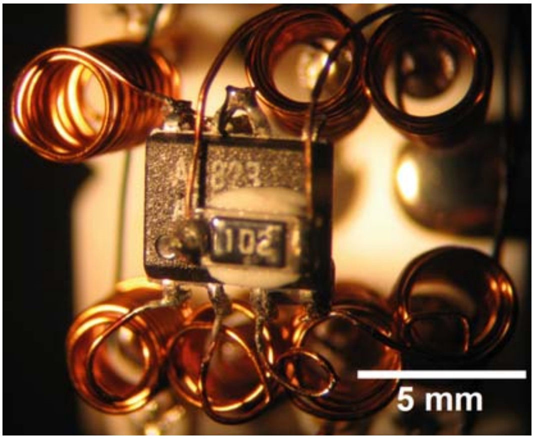

Fig. 6.13. A low temperature preamplifier (AD 823 [45]) with an attached heating resistor

6 mW – tolerable in many 4 K microscopes. The manufacturer quotes a minimal operating temperature of 233 K, but experience shows that the device already works at around 130 K. To keep the amplifier at this temperature in a 4 K environment, it is important to isolate it thermally from the 4 K parts. As can be seen in the photograph, this is achieved by connecting the chip with wire loops wound from a copper alloy with low heat conduction. When the amplifier does not operate, the temperature falls to the one of the 4 K environment. The charge carriers freeze out at this temperature and turning on power will not cause a current flow. The 1 kΩ resistor that is glued onto the SMD type plastic case is used to "jump-start" the amplifier from cold temperatures. When applying about 5 V to the heating resistor, after about 1 min, the quiescent current starts to flow and the heater can be turned off – the amplifier keeps itself warm by its power dissipation. The buffer capacitors (0.1 μF) are also glued to the amplifier case, because ceramic capacitors might only have 4% of their nominal capacitance at 4 K. The 100 MΩ feedback resistor, in contrast, is mounted firmly to a 4 K connection to minimize Johnson noise [46].

6.3 Applications

The applications of the qPlus sensor are potentially all the cases of traditional AFM. Combined STM and AFM is a special feature of qPlus technology.

6.3.1 Own Results

Initially, the main objective to utilize small amplitude AFM and qPlus technology was to see how far the spatial resolution of AFM could be taken. In 2000, subatomic resolution, that is, the resolution of spatial features within a single atom, was performed as can be seen in Fig. 6.14a [43]. Figure 6.14b shows the first result of atomic resolution by lateral AFM, also obtained using a qPlus sensor [39]. Sub-Angstrom resolution by AFM has been obtained in 2004 by operating a qPlus sensor in a higher harmonic mode [48], see Fig. 6.14c. When oscillation amplitudes are very small, the tunneling current between a conductive tip and a sample is quite large and simultaneous STM and AFM is easy to do. Surprisingly, STM and AFM yield different image data as can be seen in Fig. 6.14d [49]. Finally, the forces that act during atomic manipulation have been measured in a collaboration between the IBM Almaden Research Laboratory and our group [50]. Figure 6.14e shows the lateral force data acting between a metallic tip and a Co adatom. Note that the height difference between the last and second last force curve is only 5 pm.

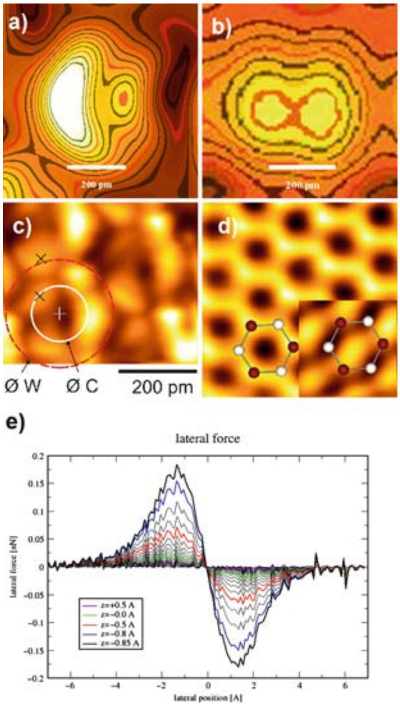

Fig. 6.14. (**a**) First sub-atomic resolution data, showing two maxima in the image of a single atom that are explained by the orbital structure of the tip [43], (**b**) a dual maximum in lateral force microscopy caused by a tip that oscillates laterally [39], (**c**) sub-Angstrom resolution using higher harmonic AFM [48], (**d**) simultaneous STM and AFM on graphite [49], and (**e**) lateral forces over a cobalt adatom [50 and Markus Ternes et al.'s chapter in this book]

6.3.2 External Groups

One of the first groups who adapted the qPlus principle was King et al. [51,52] who imaged DNA in ambient conditions. Several companies have implemented the qPlus sensor in their microscopes (see Fig. 6.15). Udo Schwarz from Yale University and Markus Heyde from the Fritz-Haber Institute in Berlin also utilized the qPlus principle (see also their chapters in this book).

6.4 Outlook

Einstein's request to make things as simple as possible is appealing and promises to not only simplify the technique, but also might help to perform new types of experiments. The question is whether force sensing can be made even simpler – or whether some things have already been made too simple.

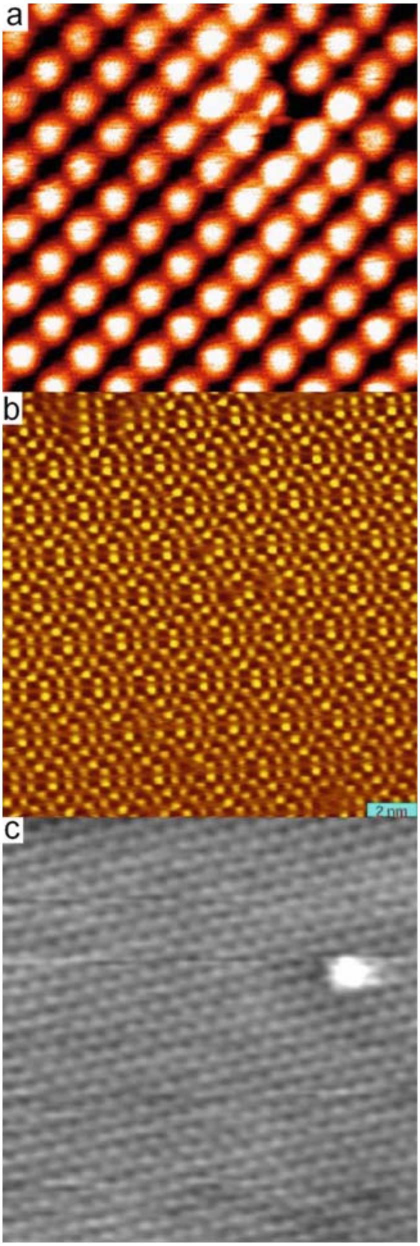

Fig. 6.15. Results obtained by commercial manufacturers of scanning probe microscopes: (**a**) Topographic image of NaCl imaged with the Omicron QPlus LT STM/AFM at 5 K showing an atomic defect [53]. (**b**) Constant-height frequency shift image of Si(111)-(7×7) imaged with an RHK 300 UHV STM/AFM (tuning fork configuration) [61]. (**c**) Constant-height frequency shift image of a Cu (111) surface with a defect imaged with a Createc UHV LT STM/AFM using a qPlus sensor [62]

This question will be answered in the future when more scientists start to look into the forces that act in atomic science and engineering. Various new results were derived with the qPlus sensor that would be difficult to obtain with traditional FM-AFM. With the commercial availability of the qPlus sensor and other research groups using it (see Chaps. 5, 7 and 9 of this book), it can be expected that further progress will be obtained, for example, when the thriving field of STM studies on surfaces is enriched with the force aspects that occur in parallel.

Acknowledgment

I wish to thank my students Stefan Hembacher, Markus Herz, Martina Schmid, Martin Breitschaft, Elisabeth Köstner, Thorsten Wutscher, Martin Smolka, Maximilian Schneiderbauer as well as the post doctoral fellows Hartmut Bielefeldt, Toyoaki Eguchi, and Sebastian Gritschneder for helping to bring qPlus AFM to its current status. McKinsey & Company, Inc. as well as T.W. Hänsch have supported the first steps towards the creation of the qPlus sensor and Jochen Mannhart from Augsburg University provided support and freedom to explore the key possibilities of small-amplitude AFM.

References

1. G. Binnig, C.F. Quate, C. Gerber, Phys. Rev. Lett. **56**, 930 (1986)
2. T.R. Albrecht, S. Akamine, T.E. Carver, C.F. Quate, J. Vac. Sci. Technol. A **8**, 3386 (1990)
3. S. Akamine, R.C. Barrett, C.F. Quate, Appl. Phys. Lett. **57**, 316 (1990)
4. O. Wolter, T. Bayer, J. Greschner, J. Vac. Sci. Technol. **9**(2), 1353 (1991)
5. L. Berlin, *The man behind the microchip: Robert Noyce*, 1st edn. (Intel, Santa Clara, USA, 2005)
6. D. Rugar, P. Hansma, Physics Today **43**(10), 23 (1990)
7. W.A. Hofer, A.J. Fisher, R.A. Wolkow, P. Grutter, Phys. Rev. Lett. **87**, 236104 (2001)
8. F.H. Stillinger, T.A. Weber, Phys. Rev. B **31**(8), 5262 (1985)
9. R. Perez, I. Stich, M.C. Payne, K. Terakura, Phys. Rev. B **58**, 10835 (1998)
10. N.W. Ashcroft, N.D. Mermin, *Solid State Physics* (Saunders College, Philadelphia, 1981)
11. Y. Martin, C.C. Williams, H.K. Wickramasinghe, J. Appl. Phys. **61**(10), 4723 (1987)
12. T.R. Albrecht, P. Grutter, H.K. Horne, D. Rugar, J. Appl. Phys. **69**, 668 (1991)
19\. F.J. Giessibl, Science **267**(5194), 68 (1995)
14. F.J. Giessibl, S. Hembacher, M. Herz, C. Schiller, J. Mannhart, Nanotechnology **15**, S79 (2004)
15. F.J. Giessibl, in *Noncontact Atomic Force Microscopy*, ed. by S. Morita, R. Wiesendanger, E. Meyer (Springer Berlin Heidelberg New York, 2002), chap. 2, pp. 11–46
16. F.J. Giessibl, Phys. Rev. B **56**, 16010 (1997)

17. M. Lantz, H.J. Hug, R. Hoffmann, P. van Schendel, P. Kappenberger, S. Martin, A. Baratoff, H.J. Guentherodt, Science **291**, 2580 (2001)
18. T. Eguchi, Y. Fujikawa, K. Akiyama, T. An, M. Ono, T. Hashimoto, Y. Morikawa, K. Terakura, T. Sakurai, M. Lagally, Y. Hasegawa, Phys. Rev. Lett. **93**(26), 266102 (2004)
19. U. Duerig, H.P. Steinauer, N. Blanc, J. Appl. Phys. **82**, 3641 (1997)
20. F.J. Giessibl, Rev. Mod. Phys. **75**(3), 949 (2003)
21. S. Hembacher, F.J. Giessibl, J. Mannhart, Appl. Surf. Sci. **188**, 445 (2002)
22. E. Momosaki, Proc. 1997 IEEE Interntl. Freq. Contr. Symp. **56**, 552 (1997)
23. F.L. Walls, in *Precision Frequency Control*, ed. by E. Gerber, A. Ballato (Academic Press, Orlando a.o., 1985), pp. 276–279
76. C.J. Chen, *Introduction to Scanning Tunneling Microscopy* (Oxford University Press, New York, 1993)
25. P. Guethner, U.C. Fischer, K. Dransfeld, Appl. Phys. B **48**, 89 (1989)
26. K. Karrai, R.D. Grober, Appl. Phys. Lett. **66**(14), 1842 (1995)
27. J. Rychen, T. Ihn, P. Studerus, A. Herrmann, K. Ensslin, Rev. Sci. Instr. **70**(6), 2765 (1999)
28. J. Rychen, T. Ihn, P. Studerus, A. Herrmann, K. Ensslin, H.J. Hug, P.J.A. van Schendel, H.J. Guentherodt, Rev. Sci. Instr. **71**, 1695 (2000)
29. J. Rychen, T. Ihn, P. Studerus, A. Herrmann, K. Ensslin, H.J. Hug, P.J.A. van Schendel, H.J. Guentherodt, Appl. Surf. Sci. **157**(4), 290 (2000)
30. K. Dransfeld, U. Fischer, P. Guethner, K. Heitmann, US Patent 5212987 (1991)
31. J. Rychen, Combined low-temperature scanning probe microscopy and magneto-transport experiments for the local investigation of mesoscopic systems. Ph.D. thesis, ETH Zuerich, Switzerland, ETH Diss No. 14119 (2001)
32. F.J. Giessibl, Appl. Phys. Lett. **76**, 1470 (2000)
33. M. Heyde, M. Kulawik, H.P. Rust, H.J. Freund, Rev. Sci. Instrum. **75**(7), 2446 (2005)
34. F.J. Giessibl, German Patent p. DE 196 33 546 (1996)
35. F.J. Giessibl, US. Patent pp. 6, 240, 771 (2001)
36. F.J. Giessibl, Appl. Phys. Lett. **73**, 3956 (1998)
37. CeramTec, CeramTec AG, Marktredwitz, Germany (2008)
38. EpoTek, Norwood, MA 02062-9106, U.S.A., (2008)
39. F.J. Giessibl, M. Herz, J. Mannhart, Proceedings of the National Academy of Sciences (USA) **99**(19), 12006 (2002)
40. M. Smolka. Rasterkraftmikroskopie. Diploma Thesis, Universitaet Regensburg, Germany (2008)
41. T. Wutscher. Einkristalline spitzen fuer die rasterkraftmikroskopie. Diploma Thesis, Universitaet Regensburg, Germany (2007)
42. F.J. Giessibl, H. Bielefeldt, S. Hembacher, J. Mannhart, Ann. Phys. (Leipzig) **10**(11-12), 887 (2001)
43. F.J. Giessibl, S. Hembacher, H. Bielefeldt, J. Mannhart, Science **289**, 422 (2000)
44. M. Schmid, J. Mannhart, F.J. Giessibl, Phys. Rev. B (2008)
45. Analog Devices, One Technology Way, P.O. Box 9106, Norwood. MA 02062-9106, U.S.A., (2008)
46. P. Horowitz, W. Hill, *The Art of Electronics* (Cambridge University Press, Cambridge, New York, 1989, 2nd ed.)
47. M. Breitschaft. Low-temperature afm. Diploma Thesis, Universitaet Augsburg, Germany (2006)

48. S. Hembacher, F.J. Giessibl, J. Mannhart, Science **305**, 380 (2004)
49. S. Hembacher, F.J. Giessibl, J. Mannhart, C.F. Quate, Proc. Natl. Acad. Sci. (USA) **100**, 12539 (2003)
50. M. Ternes, C.P. Lutz, C.F. Hirjibehedin, F.J. Giessibl, A. Heinrich, Science **319**(5866), 1066 (2008)
51. G.M. King, J. G. Nunes, Rev. Sci. Instrum. **72**(11), 4261 (2001)
52. G.M. King, J.S. Lamb, J. G. Nunes, Appl. Phys. Lett. **79**(11), 1712 (2001)
53. Omicron, *Omicron UHV AFM/STM.* Omicron Nanotechnology GmbH, Limburger Str. 75, D-65232 Taunusstein, Germany (2002)
54. Nanosurf, *easyPLL, easyPLL Sensor Controller.* Nanosurf AG, Grammetstr. 14, CH-8804 Liestal (2002)
55. K. Kobayashi, H. Yamada, H. Itoh, T. Horiuchi, K. Matsushige, Rev. Sci. Instrum. **72**(12), 4383 (2001)
21. R. Bennewitz, C. Gerber, E. Meyer, Appl. Surf. Sci. **157**(4), 207 (2000)
23. C. Barth, M. Reichling, Nature **414**, 54 (2001)
63. A. Livshits, A. Shluger, A. Rohl, Appl. Surf. Sci. **140**, 327 (1999)
71. G. Binnig, H. Rohrer, C. Gerber, E. Weibel, Phys. Rev. Lett. **50**, 120 (1983)
73. G. Binnig, H. Rohrer, C. Gerber, E. Weibel, Phys. Rev. Lett. **49**, 57 (1982)
61. RHK Technology, 1050 East Maple Road, Troy, MI 48083, USA
62. CreaTec Fischer & Co. GmbH, Industriestr. 9, 74391 Erligheim, Germany